Materials Today Bio 27 (2024) 101120

Contents lists available at ScienceDirect

Materials Today Bio

journal homepage: www.journals.elsevier.com/materials-today-bio

Fullerol-reinforced antioxidantive 3D-printed bredigite scaffold for accelerating bone healing

Jielai Yang [a,*], Zihang Zhan [b], Xingchen Li [a], Mu Hu [a], Yuan Zhu [a], Yunchao Xiao [b,**], Xiangyang Xu [a,***]

[a] Department of Orthopedics, Shanghai Institute of Traumatology and Orthopaedics, Shanghai Key Laboratory for Prevention and Treatment of Bone and Joint Diseases, Ruijin Hospital, Shanghai Jiao Tong University, Shanghai, 200025, PR China
[b] College of Materials and Textile Engineering, Jiaxing University, Jiaxing, 314001, Zhejiang Province, PR China

ARTICLE INFO

Keywords:
3D-printing
Bredigite scaffold
Fullerol nanoparticle
Reactive oxygen species
Bone regeneration

ABSTRACT

Reactive oxygen species play a vital role in tissue repair, and nonequilibrium of redox homeostasis around bone defect can compromise osteogenesis. However, insufficient antioxidant capacity and weak osteogenic performance remain major obstacles for bone scaffold materials. Herein, integrating the mussel-inspired polydopamine (PDA) coating and 3D printing technologies, we utilized the merits of both osteogenic bredigite and antioxidative fullerol to construct 3D-printed porous, biodegradable acid-buffering, reactive oxygen species (ROS) -scavenging and robust osteogenic bio-scaffold (denoted "FPBS") for in situ bone defect restoration under oxidative stress microenvironment. Initially, fullerol nanoparticles were attached to the surface of the bredigite scaffold *via* covalently inter-crosslinking with PDA. Upon injury, extracellular ROS capturing triggered the oxidative degradation of PDA, releasing fullerol nanoparticles to enter into cells for further intracellular ROS scavenging. *In vitro*, FPBS had good biocompatibility and excellent antioxidative capability. Furthermore, FPBS promoted the osteogenesis of stem cells with significant elevation of osteogenic markers. Finally, *in vivo* implantation of FPBS remarkably enhanced new bone formation in a rat critical calvarial defect model. Overall, with amelioration of the ROS microenvironment of injured tissue and enhancement of osteogenic differentiation of stem cells simultaneously, FPBS may hold great potential towards bone defect repair.

1. Introduction

The local microenvironment of the body is crucial for tissue repair and disease treatment, which remarkably influences various cellular functionalities, i.e. cell proliferation, differentiation and apoptosis [1–3]. Reactive oxygen species (ROS) is one of the main microenvironment factors, mainly including hydrogen peroxide (H_2O_2), superoxide anions ($O_2\cdot$), and hydroxyl radicals (·OH), which can induce oxidative stress and inhibit cell viability [4]. Tissue repair is a dynamic process involving interaction between cells and the surrounding matrix. This dynamic communication inspires the design of biomaterials to adapt to local cellular change while modulating its property according to the alteration of local biological signals [5–7]. To date, a variety of functional biomaterials have been developed to alleviate the local level of ROS and inflammation, thus regulating the pathological microenvironment to achieve effective tissue repair [8,9].

Severe bone defects caused by trauma, tumours, and congenital deformity remain a great challenge in the clinic, often unable to heal spontaneously through body repair mechanisms [10]. It is believed that the microenvironment of bone defects is often acid and inflamed, accompanied by the production of a large amount of ROS [11,12]. Additionally, introducing implanted materials into bone defects may reduce the production of antioxidant enzymes in the surrounding tissues of the implant, while increasing lipid peroxidation [13]. The elevated ROS caused by external and internal stimuli exacerbate local inflammation, inhibit osteoblast activity, and promote osteoclast activity, thereby hindering bone repair [14,15]. As such, previous studies have incorporated antioxidants, such as metal ions [16], small molecules [17], polymers [18], and composite coatings [19] into bone grafts to construct ROS-modulating implants for enhanced bone regeneration.

* Corresponding author.
** Corresponding author.
*** Corresponding author.
E-mail addresses: yjl12388@rjh.com.cn (J. Yang), yunchao.xiao@zjxu.edu.cn (Y. Xiao), xxy10733@rjh.com.cn (X. Xu).

https://doi.org/10.1016/j.mtbio.2024.101120
Received 6 March 2024; Received in revised form 14 May 2024; Accepted 8 June 2024
Available online 9 June 2024

Bredigite ($Ca_7MgSi_4O_{16}$) is a bioactive ceramic containing calcium, silicon, and magnesium ternary components, which has excellent biocompatibility, mineralization ability, and biological activity [20–22]. The calcium, magnesium, and silicon ions released during the bredigite scaffold degradation can promote osteogenic differentiation, osteoblast proliferation, and angiogenesis of stem cells. Compared to the acid microenvironment caused by some polymer degradation, the degradation of bredigite scaffold would generate a slightly alkaline microenvironment, which is more suitable for cell proliferation and differentiation, and has anti-inflammatory and antibacterial effects [23]. Compared to traditional inorganic bioceramic materials such as hydroxyapatite, β-tricalcium phosphate (β-TCP) et al., bredigite seems to be a better osteogenic scaffold material. Although bredigite scaffold materials can modulate the acidic microenvironment of bone defects, they cannot remove excessive ROS in the local area, and thus exhibit limited ability to regulate the pathological microenvironment of bone defects.

Fullerol, the derivative of C60, is a powerful antioxidant. Its antioxidant performance is closely related to the number and position of hydroxyl groups [24–26]. Presently, the exact mechanism by which fullerol removes ROS remains unclear. The "cage capture" theory accepted by the mainstream sticks that ROS adheres to the fullerene surface and are cleared via delivering electrons to the inner core, like the ROS elimination via superoxide dismutase [27]. Compared to other similar nanomaterials, such as carbon nanotubes and graphene, fullerol has better biocompatibility, and it has good therapeutic effects towards bacterial infections [28], chemotherapy side effects [29], degenerative disorders [30,31], and myocardial infarction [32]. Moreover, fullerol displays the capability to promote osteogenesis while inhibiting osteoclast activity, which has great potential for applications in bone tissue engineering [33,34]. However, pure fullerol nanoparticles are too small to remain in local areas for a long time and are not suitable for bone repair application. Therefore, integrating fullerol with other biological scaffolds can effectively regulate the ROS microenvironment and achieve better bone defect repair.

In this study, using mussel-inspired polydopamine (PDA) coating technology, the 3D bredigite scaffold is stably combined with fullerol through self-assembly crosslinking, constructing a multifunctional scaffold with stable ROS clearing, acidic buffering, and excellent osteogenic performance to achieve efficient in situ repair of bone defect (Fig. 1). In the ROS microenvironment, extracellular ROS clearance triggers PDA degradation, releasing fullerol nanoparticles to enter the cell to further regulate intracellular ROS. To begin with, the cytotoxicity and antioxidant performance of FPBS was studied. Then, the in vitro osteogenic performance of FPBS was studied. Finally, the *in vivo* bone repair performance of FPBS was verified in a rat critical calvarial defect model.

2. Experimental section

2.1. Materials

Fullerol was purchased from Tanfeng Graphene Technology Co., Ltd. (Suzhou, China); Bredigite was obtained from Zhenghai Biological Co., Ltd. (Yantai, China); All other reagents were purchased from Sigma-Aldrich.

2.2. Preparation of 3D-printed bredigite scaffold

The 3D-printed bredigite scaffold is produced similar to our previous report [35]. Briefly, using ethyl silicate, magnesium nitrate hexahydrate, and calcium chloride as raw materials, the bredigite powder is prepared by sol-gel method. The bredigite powder, resin and various additives were mixed to prepare the printing ink. Then, the designed bracket model was converted into STL format and imported into the printer, followed by printing parameter settings, including scanning speed, laser power, and laser radius. Afterwards, the prepared printing ink was loaded, and the printing was executed to obtain the scaffold embryo. Finally, the scaffold embryo was subjected to high-temperature sintering (1150–1450 °C, 3–4 h) to obtain the bioceramic bredigite scaffold (Bre).

2.3. Modification of fullerol nanoparticles on the bredigite scaffold

To modify the surface of bredigite scaffold with fullerol nanoparticles, the 3D-printed scaffold was sterilized with 75 % ethanol. After the ethanol evaporated, the scaffold was immersed in a mixed solution (pH = 8.5) of fullerol (1 mM), polydopamine (2 $mg{\cdot}mL^{-1}$), and tris-HCl (10 mM). After gently shaking for 12 h, the scaffold was moved out and cleaned with deionized water three times, dried to harvest the fullerol-modified bredigite scaffold (Bre@PDA-Ful). For comparison, a polydopamine-modified bredigite scaffold (Bre@PDA) was also prepared through the same procedure.

2.4. Scaffold characterization

(1) Scanning electron microscope (SEM): the SEM (S-4800; Hitachi, Kyoto, Japan) was used to examine the morphology of the scaffold surface. Before examination, the scaffold was coated with gold, and the microstructure image of the scaffold surface was obtained under an accelerating voltage of 10 kV. (2) Fourier transform infrared spectroscopy (FTIR): the chemical bond of scaffold material was measured using an FTIR (Nicolet 6700; Thermo Scientific, USA). For each test, 128 scans were recorded with a wavelength of 650∼4000 cm^{-1} and a resolution of 4 cm^{-1}. (3) X-ray photoelectron spectroscopy (XPS): the chemical composition of materials was analyzed using XPS (Thermo Scientific Escalab 250Xi) (4) Contact angle measurements (WAC): the hydrophobic or hydrophilicity nature of the scaffold was examined using a WAC Surface Analysis System (DSA25S, Data Physics Corporation). (5) Mechanical analysis: the scaffold is placed on an electronic universal testing machine for mechanical testing, and tested at room temperature using a 1 kN sensor with a compression rate of 1 mm/min (6) Degradation test: the scaffold was immersed in a simulated solution, and taken out for weighing on day 3, day 7, day 14, day 21, day 28, and day 35, respectively.

The degradation rate (%) = $(Mo\text{-}M_1)/Mo * 100\%$

Mo is the initial mass and M_1 is the remaining mass at each time point. At the same time, the pH value of the solution at each time point is tested by a pH meter.

2.5. Viability and proliferation assessment

Before culturing cells, the scaffolds were disinfected with ethanol(wt % ∼75 %), and then soaked overnight in the culture medium. The scaffold was placed in a 24-well culture dish and cells were inoculated onto the scaffold with a cell density of $2*10^4$ mL^{-1}. The dish was transferred in an incubator at 37 °C (95 % humidity and 5 % CO_2). The culture medium was changed every two days. At each time point, live/dead staining was used for the evaluation of cell viability. Besides, the cells on scaffolds at days 1, 4 and 7 were treated sequentially with 4 % paraformaldehyde, 0.1 % Triton X-100 and 4 % bovine serum albumin (BSA). F-actin and nucleus were stained with Phalloidin FITC and DAPI for 10 min, respectively, and then recorded under a confocal laser scanning microscope (CLSM). Cell proliferation was measured using the CCK-8 test. On days 1, 4 and 7, CCK-8 solution was added and incubated for 2 h, and the obtained solution was measured using an ultraviolet spectrophotometer at a wavelength of 450 nm.

2.6. Antioxidant activity measurement

Firstly, total antioxidant capacity was measured using ABTS reagent. The scaffold sample was mixed with rapid ABTS reagent, incubated at room temperature for 5 min, and detected at a wavelength of 414 nm. Further, intracellular ROS detection was conducted. The scaffold with a cell concentration of $1*10^4$ was incubated with 100 μM H_2O_2 for 2 h, and then dichlorofluorescein diacetate was added. The fluorescence image was obtained using CLSM.

2.7. Osteogenic activity assessment

Reverse Transcription-Polymerase Chain Reaction (RT-PCR) was first performed for assessment of osteogenic activity After incubation for 7 days, cells were harvested, and total RNA were extracted, followed by reverse transcription and amplification of the targeted gene fragments. The primer sequences of the target genes are listed in Table S1. The expression of targeted gene was standardized to that of β-actin. To visually demonstrate the osteogenic activity, immunofluorescence of the scaffold was observed. At day 4, the cells were treated sequentially with 4 % paraformaldehyde, 0.1 % Triton X-100 in PBS, and 5 % BSA. Afterwards, the cells were stained overnight with polyclonal antibodies (BMP2, OCN and COL1A1) (1:100 dilution) at 4 °C. Subsequently, the cells were incubated with goat anti-rabbit lgG-Cy3 (secondary antibody) and DAPI was used to stain the nuclei.

2.8. In vivo bone healing evaluation

Primarily, a critical bone defect model was established. The animal experiment has been approved by the Animal Ethics Committee of Ruijin Hospital Affiliated to Shanghai Jiaotong University School of Medicine. 16 Sprague Dawley rats (approximately 220 g) were randomly divided into four groups: Blank group, Bre group, Bre@PDA group, and Bre@PDA-Ful group. After general anaesthesia, routine skin preparation and disinfection were performed. A 1.5 cm sagittal incision was made on the middle skin of head, and dissected to expose the skull. Remove the circular bone block with a 5 mm ring drill on the bilateral skull. Then, different scaffolds were implanted separately, and the blank group only needed to drill holes without scaffold implantation. At 8 weeks after surgery, the rats were euthanized to obtain skull specimens for further experiments.

Afterwards, the obtained skull specimens were detected using Micro-CT after immersing them in a 4 % polyformaldehyde buffer solution for 2 h. The scanning parameters were set as 70 kV, 114 μA, 700 ms integration time, and the physical resolution of each pixel in the scanning area is 18 μm. The area of interest is set as a 250 μm circular area around the graft, and quantitative data on relative bone volume (BV/TV), BMD, and porosity are measured within the VOI using Micro-CT built-in software.

Furthermore, immunohistochemical evaluation, including HE staining, Van Gieson staining and Alizarin red/Calcein staining was implemented to characterize the bone repair effect.

For HE staining, the harvested specimens were treated 10 % paraformaldehyde, followed by incubation with 10 % formic acid at room temperature for 7 days. The morphology of new bone were tested under a microscope.

For Van Gieson staining, the harvested specimens were subjected to ethanol gradient dehydration, transparency, defatting, and embedding, and then cut into 200 μm thick hard tissue sections using a slicing machine. A 50 μm thick periosteal slice was obtained by polishing with a grinding machine. After routine Van Gieson staining, the morphology of the new bone tissue at the defect site was observed under microscope.

For Alizarin red/Calcein staining, the procedures were as followes: firstly, alizarin red fluorescein (30 mg/kg) was subcutaneously injected into the neck of rats at 2 weeks after surgery. Secondly, the first injection of calcein fluorescein (6 mg/kg) was administered at 4 weeks after surgery, and the second injection of calcein fluorescein (6 mg/kg) was administered at 6 weeks after surgery. Thirdly, after 8 weeks of surgery, skull specimens were harvested, fixed with 10 % paraformaldehyde, dehydrated, transparent, defatted, and embedded. Periosteal slices of 50 μm thick were obtained using a hard tissue slicer, observed under light microscope.

Finally, immunohistochemical analysis was conducted. The samples were sequentially treated with xylene, gradient alcohol, and citrate buffer solution. Afterwards, the sample was incubated with primary antibody at 4 °C overnight, incubated with the secondary antibody at 37 °C for 1 h.

2.9. Statistic analysis

The experimental data was analyzed via GraphPad Prism 8.0 software, and the data were shown as the means ± SD. The Student's t-test was performed for inter-group comparison, and $P < 0.05$ suggests a statistically significant difference.

3. Results and discussion

3.1. Fabrication and characterization of FPBS

To fabricate FPBS, a bredigite scaffold (Bre) was first produced by 3D printing method and high-temperature sintering (Fig. 1a). After that, PDA and fullerol have coated the surface of bredigite scaffold *via* covalent bonding to obtain PDA and fullerol-modified bredigite scaffold (Bre@PDA-Ful) (Fig. 1b). The byssus of marine mussels can secret adhesive protein that rich in 3′4′-dihydroxyphenylalanine (DOPA) for achieving firmly adherence to reefs and ship surfaces in seawater [36]. Inspired by this, researchers found that PDA has properties similar to mussel adhesion protein. In aqueous solution, dopamine can rapidly form super viscous PDA film on the surface of Bre scaffold through oxidation polymerization process. The surface of the PDA film contains abundant active groups, e. g. catechol and amino groups, which can easily undergo Schiff base or Michael addition reactions with functional groups, thereby endowing the scaffold surface with multiple functionalities [37,38]. With a large number of hydroxyl groups, fullerol have good solubility and are easily grafted by covalent bonding with PDA film.

The general view of the 3D printed porous bredigite scaffold is shown in Fig. 2a, and its internal morphology and pores are regular and uniform. The surface of the bredigite scaffold without PDA modification is white, while the colour darkens in the PDA groups (including Bre@PDA and Bre@PDA-Ful groups). SEM results showed the surface morphology of each scaffold. However, considering the PDA film and fullerol are both in nanoscale, so there is no significant difference in the morphology of the three groups (Fig. 2b). The FTIR results showed the absorption bands at 980-1000 cm^{-1}, 890-910 cm^{-1}, and 840-860 cm^{-1}, which are the characteristic Si–O bands in the bredigite scaffold. There is no significant difference among the three groups as the surface coating component, i.e. PDA and fullerol, takes a small proportion (Fig. 2c). XPS results showed that the (N1s, 412.5eV) peak in the Bre group remarkably elevates compared to that in the Bre@PDA group, which is caused by the presence of amine and amide bonds in PDA coating. Additionally, it can be seen that although the (N1s, 412.5eV) peak increases in the Bre@PDA-Ful group compared to that in Bre group, the peak value decreases when compared to that in the Bre@PDA group. This is largely due to the introduction of fullerol which dilutes the nitrogen amount in the PDA coating (Fig. 2d). These results indicate that PDA and fullerol have been successfully modified on the surface of the bredigite scaffold.

Subsequently, we investigated the mechanical properties of the fabricated scaffolds. The average compressive modulus of three groups is 12.5 ± 0.3, 12.3 ± 0.5, and 12.1 ± 0.6, respectively. There is no significant difference among three groups ($P > 0.05$), indicating PDA-Ful modification has little effect on the mechanical strength of the

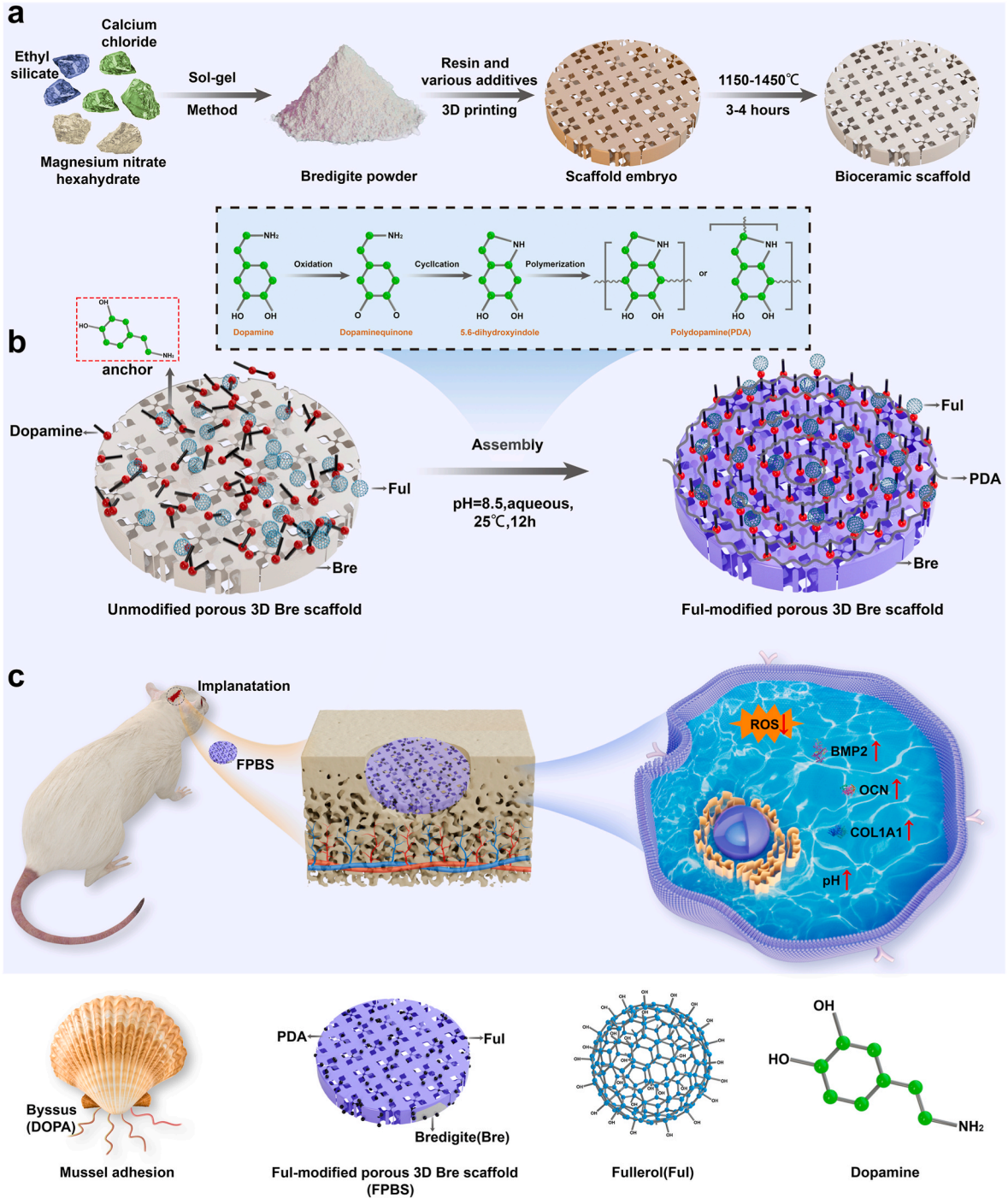

Fig. 1. a) Diagram for the production of 3D bredigite scaffold. b) The process of modifying fullerol onto bredigite scaffold using PDA as the crosslinking medium. Mussels secret adhesion proteins that are rich in 3′4′-dihydroxyphenylalanine (DOPA), achieving robust attachment on the different surfaces in an aquatic environment. Inspired by this, the FPBS is prepared by PDA coating technology. c) The *in vivo* bone healing schematic of FPBS, and this process involves modulating local microenvironment and osteogenic activity.

scaffold (Fig. 2e). Furthermore, the WAC of Bre@PDA (35.7 ± 4.2°) and Bre@PDA-Ful (34.7 ± 7.6) remarkably decreased compared to that of Bre group (59.0 ± 6.0°), which indicates the PDA-Ful modification effectively improving the hydrophilicity of the scaffold (Fig. 2f).

Further, the in vitro degradation test showed a similar degradation curve of the three groups, with degradation rates of 30.2 ± 3.1 %, 30.1 ± 1.3 %, and 30.2 ± 2.5 % after 5 weeks, respectively (Fig. 2g). As the scaffold degraded, the pH value of the solution gradually increased, reaching the maximum and stabilizing at 4–5 weeks. The maximum pH values of the three groups are 8.63 ± 0.04, 8.64 ± 0.06, and 8.59 ± 0.09, respectively(Fig. 2h). Obviously, the increased pH following scaffold degradation is beneficial for improving the acidic microenvironment in the defect area, which benefits cell proliferation and differentiation.

3.2. Cytocompatibility evaluation of FPBS

The cytocompatibility assay was performed to assess the biocompatibility of FPBS. BMSCs were implanted onto the scaffold and the morphology of cells on the scaffold was observed using CLSM(Fig. 3a,b).

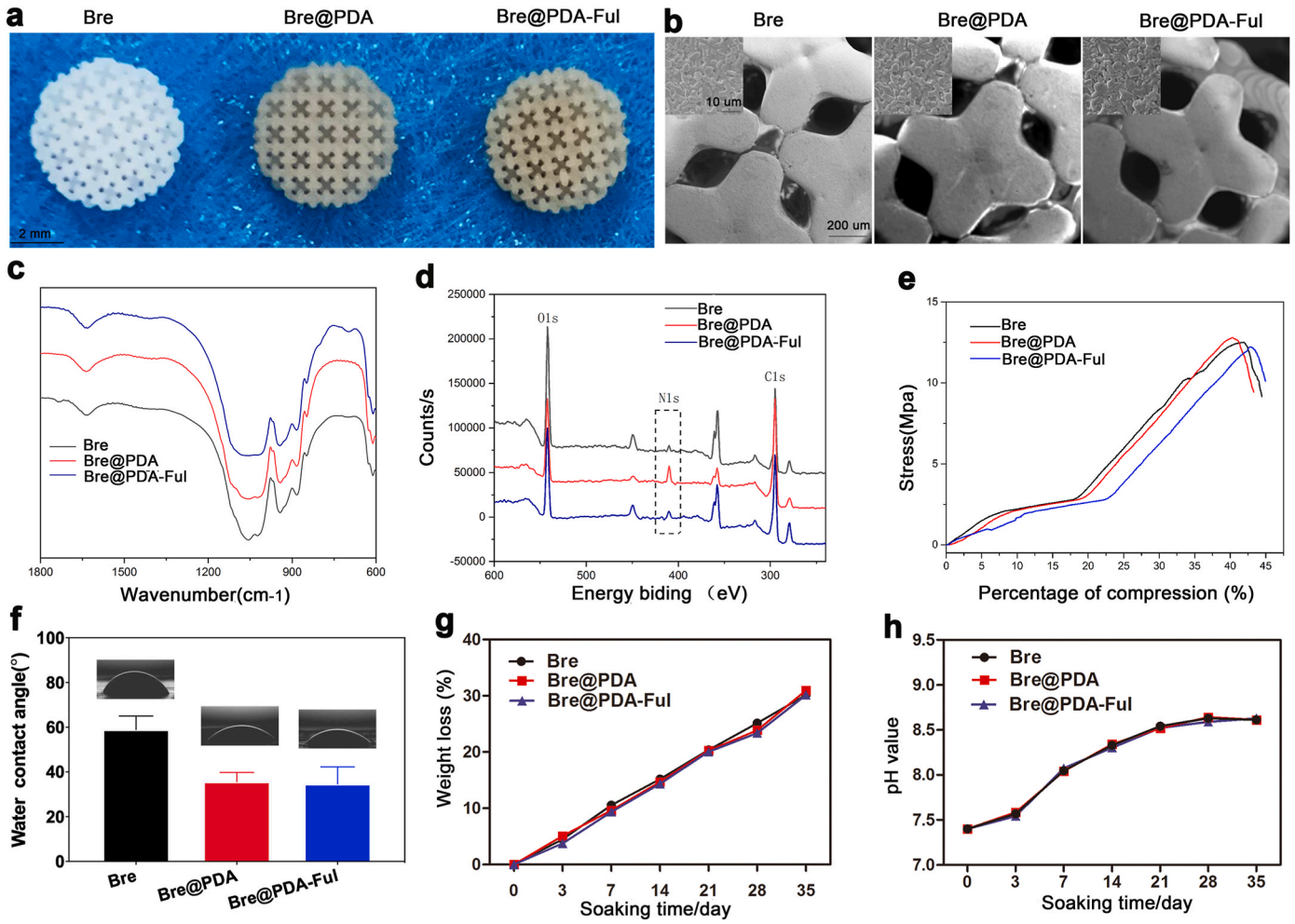

Fig. 2. Characterization of FPBS. a) Overall digital images of bredigite (Bre) scaffold, PDA-modified bredigite (Bre@PDA) scaffold, and fullerol/PDA modified bredigite (Bre@PDA-Ful) scaffold. b) SEM images of scaffolds. c) FTIR spectra of scaffolds. d) XPS spectra of scaffolds. e) Stress-compression curve of scaffolds. f) Water contact angles of scaffolds. g) Degradation cure of scaffolds. h) pH values of medium following degradation.

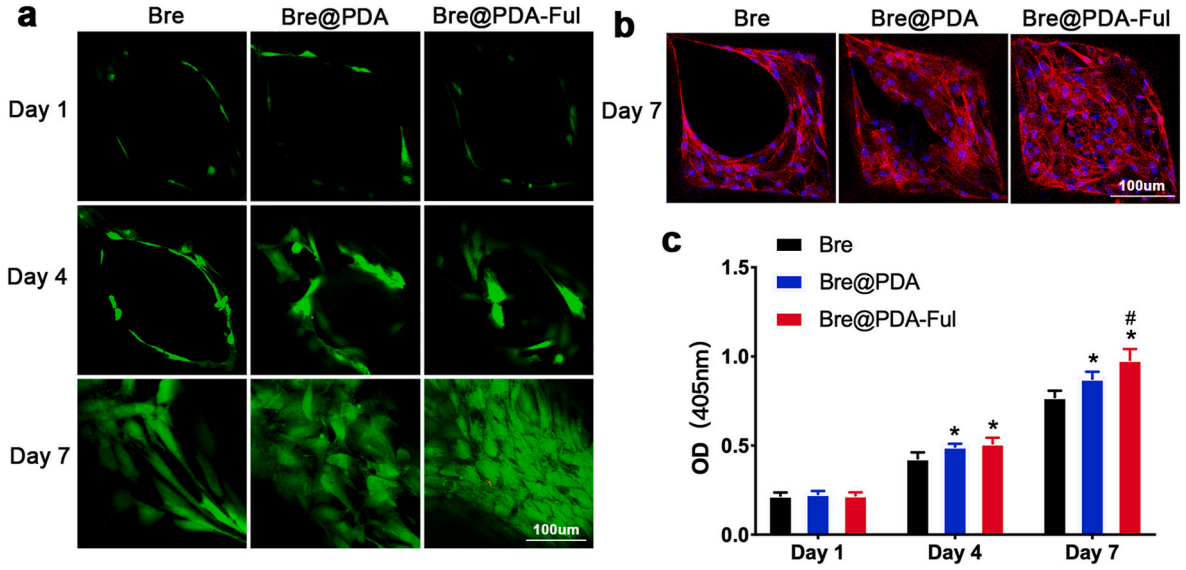

Fig. 3. Biocompatibility of FPBS. a) The representative images of live/dead staining on day 1, 4 and 7. b) The representative images of cytoskeleton staining of BMSCs on the scaffolds on day 7. c) The CCK-8 assay of BMSCs on the scaffolds at day 1, 4, and 7. (*, # indicate $P < 0.05$ comparing to day 1, and day 4, respectively).

Moreover, live/dead staining showed that the cells had not yet fully unfolded on the first day, and their morphology was relatively slender. As time went on, the cell morphology became more plump and spacious. All three scaffolds favoured cell attachment and growth, exhibiting distant variation in filopodia- and lamellipodia-like extensions with seldom dead cells. Compared to the Bre group, the cell proliferation rate of the Bre@PDA group and the Bre@PDA-Ful group significantly increased. Especially in the Ful group, cells fully covered the whole pore on day 7. The hydrophilicity of the scaffold surface was significantly improved after PDA coating, which was conducive to cell adhesion and proliferation. Although there have been varying reports on the effects fullerol on cell proliferation previously, certain amounts of fullerol have promoting effect on stem cell growth. This is probably because fullerol improves DNA synthesis *via* intracellular ROS clearance, leading to a higher cell proliferation [39]. Furthermore, CCK-8 results showed that the cell number of the Bre@PDA Group and the Bre@PDA-Ful group increased compared to that of the Bre group on day 4, and on day 7, with a significant difference among the three groups. The growth trend was particularly evident in the Bre@PDA-Ful group, which in consistent with the results of live/dead staining (Fig. 3c). Together, the FPBS has good compatibility and fullerol modification can significantly improve the viability and proliferation of implanted stem cells.

3.3. ROS scavenging capability of FPBS

ROS has a dual effect on various cellular activities, which contributes to tissue development, damage, and repair [40–42]. Moderate ROS is beneficial for tissue repair, while excessive ROS can cause cell dysfunction or even death by damaging proteins, lipids, and DNA. In particularly, excessive ROS will induce the production of a series of

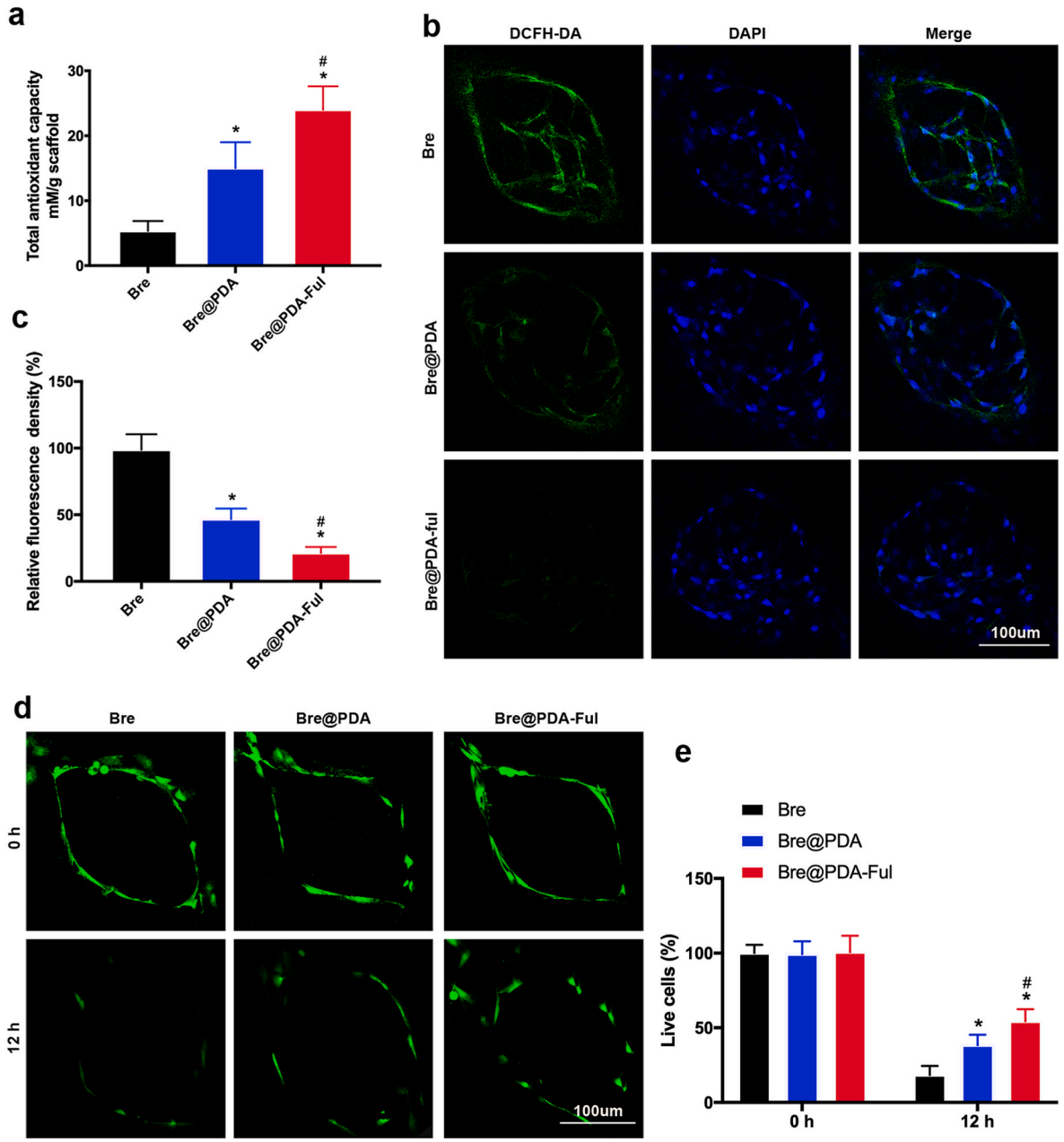

Fig. 4. Antioxidant property of FPBS. a) The total antioxidative capacity of scaffolds. b) Representative images of DCFH-DA staining following H_2O_2 treatment for 2 h. c) Representative images of the live/dead staining following H_2O_2 treatment for 12 h. d) Quantitative analysis of live cells. (*, # indicate $P < 0.05$ comparing to the Bre group, and the Bre@PDA group, respectively.)

inflammatory markers, such as IL-1、IL-6 and TNF-a, and the imbalance of redox stress based on ROS will lead to acute or chronic inflammatory diseases [43,44]. The cells at the damaged site are important factors influencing tissue repair and regeneration. However, excessive ROS can induce oxidative damage to both endogenous and exogenous cells at the injury site [45,46]. Although the Bre scaffold has good osteogenic performance, its ability to clear ROS is weak. Fullerol, as an effective free radical scavenger, can quench ROS like biological enzyme reactions. In addition, PDA, a natural biopolymer with good biocompatibility and degradation, can clear various ROS *in vivo* and *vitro*, and inhibit ROS-induced inflammation and cell apoptosis [47]. The total antioxidant capacity test was conducted to measure the extracellular ROS scavenging ability of FPBS. Results showed the total antioxidant performance of three groups as follows: Bre@PDA-Ful > Bre@PDA > Bre. This verified the ROS cleaning ability of both PDA and fullerol, and their collaborative performance was achieved in Bre@PDA-Ful (Fig. 4a). Subsequently, intracellular ROS levels were detected using fluorescent probes. It is generally believed that many nanomaterials, including fullerol, can achieve intracellular endocytosis through receptor-mediated or direct penetration [48,49]. The results showed that following H_2O_2 treatment, strong fluorescence appeared in the cells of the Bre group, indicating a large amount of ROS accumulated in cells. Compared to the Bre group, the fluorescence intensity inside cells of the Bre@PDA group and Bre@PDA-Ful group significantly reduced (Fig. 4b). The quantitative analysis of fluorescence intensity was as follows: Bre@PDA-Ful group > Bre@PDA group > Bre group (Fig. 4c). After H_2O_2 treatment (100 μM) for 12 h, the cell survival rate on the scaffold was tested to investigate the ability of FPBS to alleviate cell apoptosis under oxidative stress. The results showed that the cell survival rate was highest in the Bre@PDA-Ful group, followed by the Bre@PDA Group, and the Bre group (Fig. 4 d, e). Taken together, the Bre scaffold modified with fullerol has a dual antioxidant effect of PDA and fullerol, exhibiting excellent performance in resisting oxidative stress.

3.4. Osteogenic differentiation of stem cells induced by FPBS

Previous studies have shown that bredigite, containing Ca, Si, and Mg elements, has better osteogenic performance compared to β-TCP [21]. To verify the osteogenic performance of FPBS, osteogenic expression experiments were conducted. Due to the presence of calcium ions in the bredigite scaffold, there are interferences when conducting traditional osteogenic mineralization experiments, e.g. alizarin red test and alkaline phosphatase assay. Thus, in this study, the osteogenic differentiation of stem cells on FPBS is determined by detecting related genes or proteins. Compared with the growth medium (GM) group, the mRNA expression level of ALP, osteocalcin (OCN), runt-related transcription factor 2 (RUX2), and bone morphogenetic protein 2 (BMP2) were significantly increased in the Bre group, which confirms that bredigite itself has certain osteogenic properties. Meanwhile, expression of the genes further increased in the Bre@PDA group and Bre@PDA-Ful group, remarkably highest in the Bre@PDA-Ful group (Fig. 5a). The results of immunofluorescence were consistent with that of RT-PCR. From the fluorescence images, it can be seen that the fluorescence intensity of ALP, OCN, and BMP2 proteins was highest in the Bre@PDA-Ful group, followed by the Bre@PDA group and Bre group (Fig. 5b). Although pure bredigite scaffold has certain osteogenic capability, its osteogenic performance further improved *via* surface modification with PDA and fullerol. These results indicated that FPBS has great potential in bone repair.

3.5. In vivo bone repair of FPBS

The bone healing effect of FPBS was assessed in the rat calvarial defect (Fig. S1). After implanting the scaffold into rat calvarial defect for 8 weeks, the skull specimen was harvested for imaging and histological analysis. Micro-CT results showed that all four groups generated new bone formation to some extent. In the blank group, a small amount of new bone could be seen around the defect. All three scaffold groups had new bone on the surface. Expect some gaps on the surface of the Bre group, there were few visible gaps in the Bre@PDA group and Bre@PDA-Ful group. In addition, the osteogenesis inside the scaffold can be seen from the 2D cross-section view. Similarly, the blank only had a small amount of new bone formation in the surrounding areas, while the other three scaffold groups had new bone formation in the gaps of the scaffold, with the least void spaces in the Bre@PDA-Ful group, followed by the Bre@PDA group and Bre group(Fig. 6a). Considering that the colour of the scaffold and the newly formed bone is similar on the regular imaging, the newly formed bone was marked in yellow to be intuitively displayed. From the anteroposterior and vertical view, newly formed bones in the Bre@PDA-Ful group were remarkably higher than the other two scaffold groups (Fig. 6b). Compared to the Bone volume fracture (BV/TV) value of the blank group (9.5 ± 0.7 %), the BV/TV values of the other three scaffold groups were 22.4 ± 3.4 % (Bre), 35.3 ± 1.7 % (Bre@PDA), and 43.6 ± 2.4 % (Bre@PDA-Ful), respectively (Fig. 6c). The BV/TV value of Bre@PDA group was 1.58 fold of the Bre group, indicating that PDA modification could effetively improve the osteogenic performance. The BV/TV value of the Bre@PDA-Ful group was 1.95 fold of the Bre group, which fully demonstrated that fullerol modification further improved the osteogenic performance of the scaffold and greatly promoted bone defect healing. The reasons for this are mainly as follows: (1) Fullerol/PDA modification could greatly improve the ROS microenvironment of bone defect areas, which was conducive to the formation of new bone; (2) fullerol modification further enhanced the osteogenic differentiation of stem cells and accelerated bone repair.

Similar to BV/TV results, the bone mineral density (BMD) of the four groups exhibited a similar trend(Fig. 6d). The porosity of the scaffold was analyzed, and the results were showed as follows: Bre group (45.6 ± 3.4 %) > Bre@PDA group (25.2 ± 4.6 %) > Bre group (12.4 ± 2.9 %) (Fig. 6e). Herein, the lower porosity of the samples implied more new bone formation and indirectly reflected the better osteogenic performance of FPBS.

Histological analysis of four group samples could provide more information on the repair of the defective parts. HE staining could display newly formed bone, fibrous tissue, and vascular structures. As shown in Fig. 7a, there was little newly formed bone in the blank group, mainly fibrous tissue. A similar result was observed in the Bre group, which might be related to the imbalance of new bone formation within the scaffold. The new bone was mainly on the surface of the scaffold, and little bone formation was observed inside the scaffold. In contrast, the amount of newly formed bone in the Bre@PDA group and the Bre@PDA-Ful group significantly increased, especially in the Bre@PDA-Ful group, the scaffold pores were mostly filled with newly formed bone. Van Gieson staining was effective in highlighting the newly formed bone. From Fig. 7b, the formation of new bone in different groups could be visually observed, and the results were consistent with HE staining. By injecting the hydrophilic mineral fluorescein into the body, the rate of new bone formation can be tracked and determined, directly reflecting the bone repair of the scaffold. In principle, fluorescein binds to free calcium ions, and injected at different times, the newly formed bone at that period is labelled with specific bands. The higher the labelling rate, the more newly formed bone there is. The greater the distance between adjacent bands, the faster the bone formation rate, and vice versa [50,51]. From the staining results, it could be seen that the staining in the blank group was significantly lighter, and the distance between labelling bands was relatively narrow. In contrast, the staining of the three scaffold groups was remarkably deepened. From Bre group to Bre@PDA group, then to Bre@PDA-Ful group, there was a trend of gradually increasing staining intensity and widening staining distance in each group (Fig. 7c). Through quantitative analysis of mineral apposition rate, Fig. 7d showed the mineral apposition rate of each group in the 2nd two weeks, from high to low: Bre@PDA-Ful group > Bre@PDA group > Bre group > control group. Fig. 7e showed the mineral apposition rate of

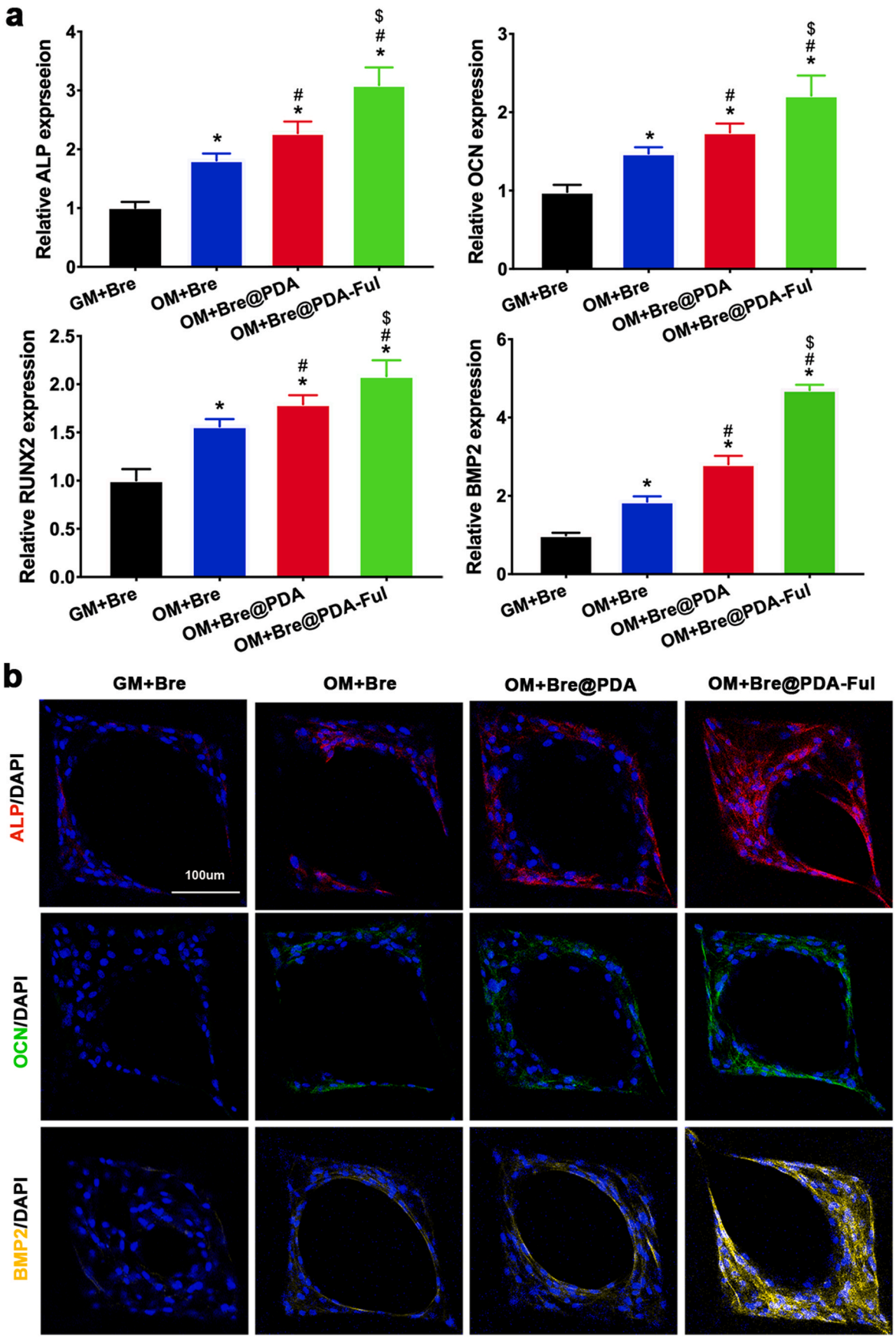

Fig. 5. The effect of FPBS on osteogenic molecule expression. a) qRT-PCR analysis of osteogenic genes, including alkaline phosphatase (ALP), runt-related transcription factor 2 (RUNX2), osteocalcin (OCN), and collagen type I (COL1A1). b) The results of immunofluorescence assay of ALP, OCN, and BMP2 in BMSCs on scaffolds at day 4. (*, #, and $ indicate $P < 0.05$ comparing to the GM + Bre group, the OM + Bre group, and the OM + Bre@PDA group, respectively.)

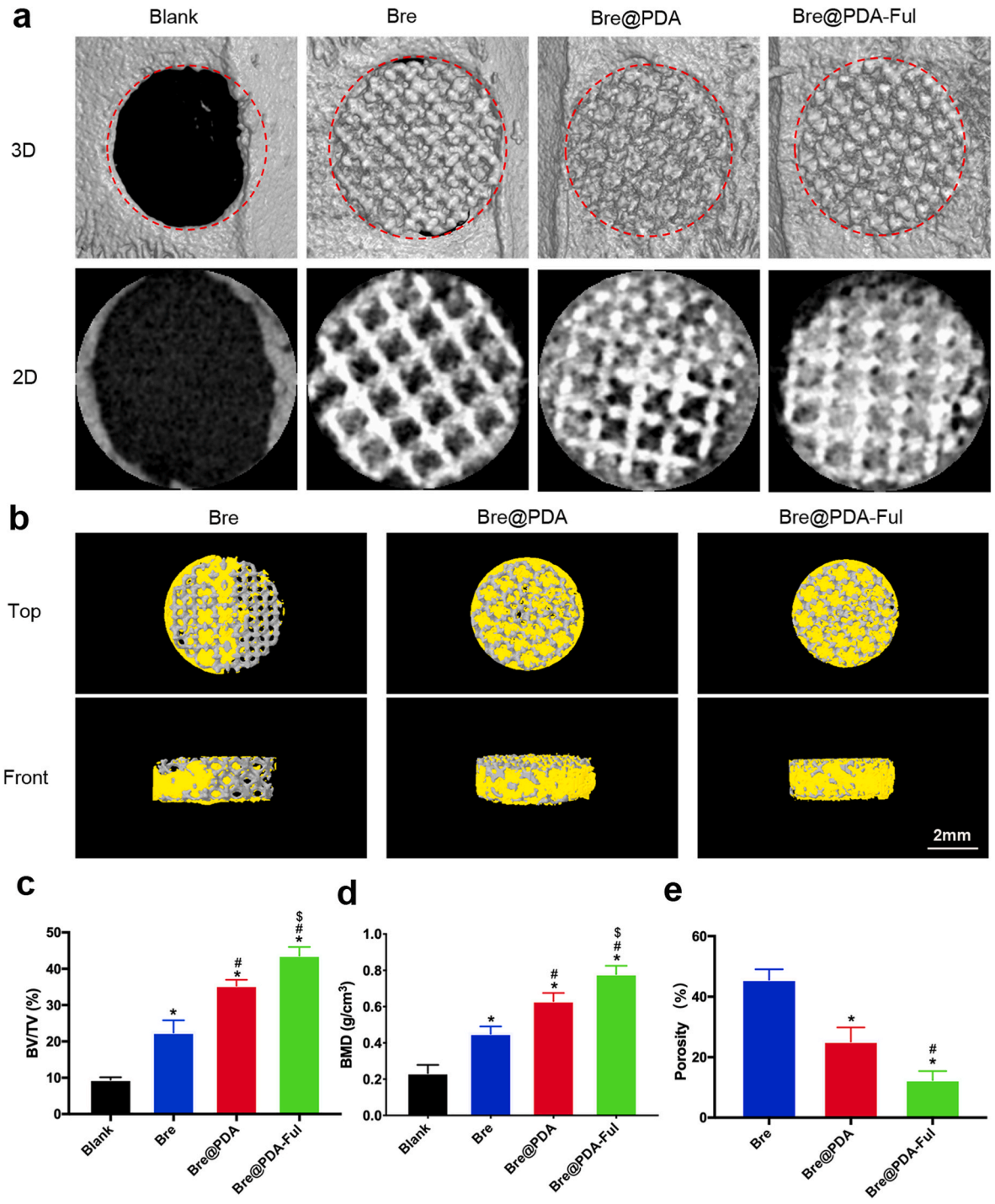

Fig. 6. Micro-CT analysis of bone healing effect of FPBS. a) The new bone formation in the defect areas (3D view and 2D view). b) The 3D images of the scaffolds. The new bone is marked in yellow. c) Bone volume fracture (BV/TV), d) Bone mineral density (BMD), and e) Porosity of defect areas in four groups. (*, #, and $ indicate $P < 0.05$ comparing to the Blank group, the Bre group, and the Bre@PDA group, respectively.). (For interpretation of the references to colour in this figure legend, the reader is referred to the Web version of this article.)

each group in the 3rd two weeks, which was consistent with the trend in the 2nd two weeks. Although the Bre@PDA group showed an upward trend compared to the Bre group, there was no statistically significant difference ($P > 0.05$). This might indicate that the bone repair in the 2nd two weeks was relatively active, displaying a significant difference between groups. The slower bone repair speed in the 3rd two weeks results in a smaller difference between the two groups.

Furthermore, the immunohistochemical experiment was conducted to evaluate the bone healing at the molecular level. Fig. 8a showed that osteogenic-related proteins, including BMP2, OCN and COL1A1, were seldom expressed in the blank group, but showed significantly stronger fluorescence intensity in the three scaffold groups, especially in the Bre@PDA-Ful group. Fig. 8b was a semi-quantitative analysis of the expression of BMP2, OCN, and COL1A1, respectively. It can be seen that the expression level was highest in the Bre@PDA-Ful group, followed by the Bre@PDA group and the Bre group. Together, the above results suggest that FPBS fully integrates the advantages of bredigite and fullerol, effectively promoting bone defect repair *in vivo*.

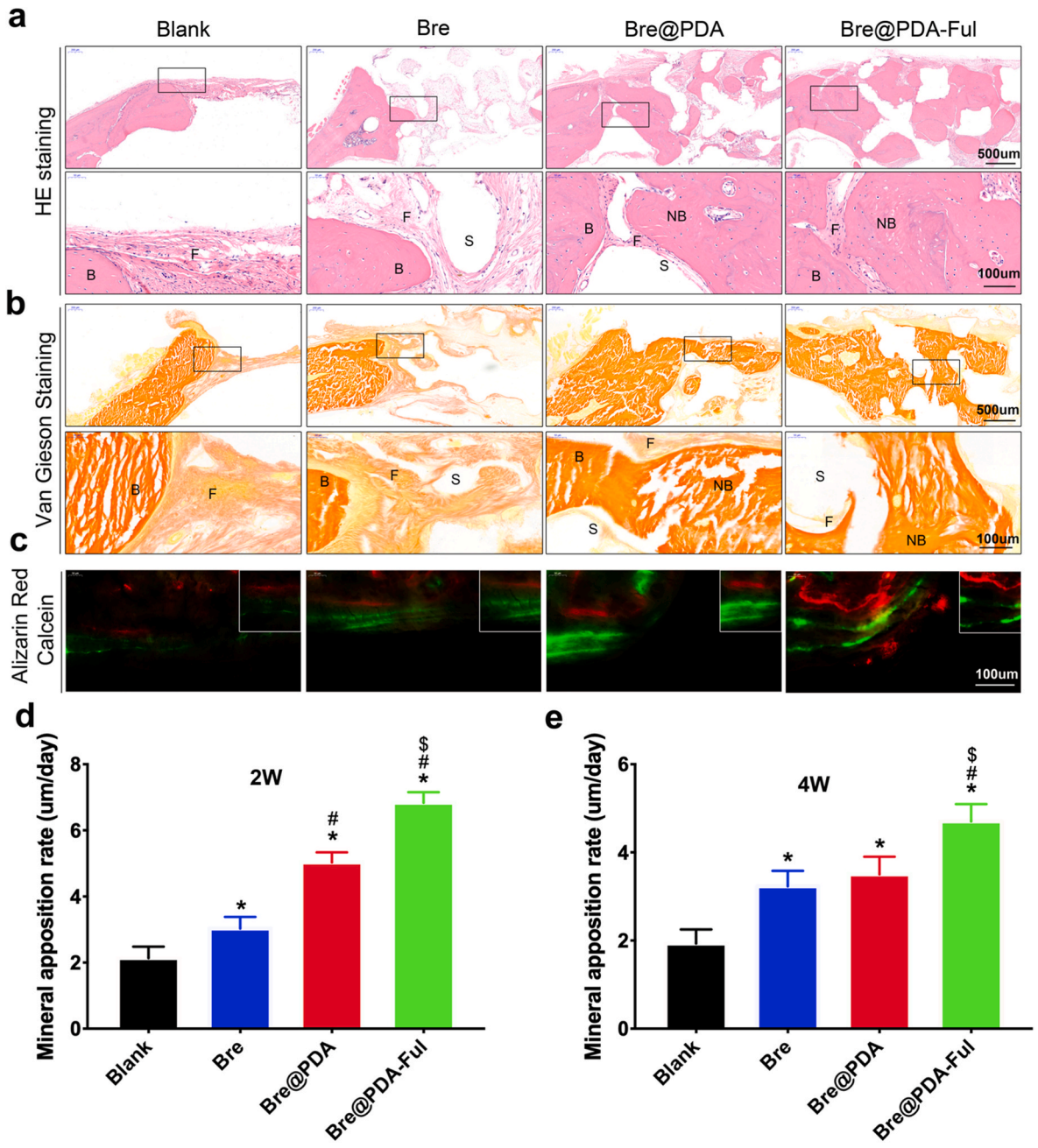

Fig. 7. Histological analysis of bone healing effect of FPBS. a) HE staining of defect area in four groups. (B: bone, F: fibrous tissue, NB: new bone, S: scaffold.) b) Van Gieson staining. c) Alizarin Red/Calcein staining, and mineral apposition rate d) at the 2nd two weeks, and e) at the 3rd two weeks. (*, #, and $ indicate $P < 0.05$ comparing to the Blank group, the Bre group, and the Bre@PDA group, respectively.). (For interpretation of the references to colour in this figure legend, the reader is referred to the Web version of this article.)

4. Conclusion

In summary, we developed a fullerol-modified bredigite scaffold using 3D printing and mussel adhesion-inspired coating technology. The developed scaffold possesses outstanding advantages of ROS scavenging, acidic buffering, and osteogenic activity, thereby accelerating the repair of bone defects. *In vitro* experiments show that FPBS has excellent antioxidant properties, providing a favorable environment for stem cell colonization and thus improving the survival rate of stem cells. Meanwhile, FPBS further promotes osteogenic differentiation of stem cells based on bredigite. The *in vivo* experiments demonstrate a remarkabe surge of new bone formation, which is due to the synergistic effect of ROS microenvironment regulation and enhanced osteogenic differentiation. To sum up, the multifunctional FPBS has greatly improved the osteogenic performance of the traditional scaffold, which may exhibit promising therapeutic effects towards some refractory bone disorders complicated with other pathological conditions, such as diabetes, osteoporosis or chronic inflammation.

CRediT authorship contribution statement

Jielai Yang: Writing – original draft, Project administration, Investigation, Funding acquisition. **Zihang Zhan:** Formal analysis, Data curation. **Xingchen Li:** Methodology, Formal analysis. **Mu Hu:** Validation, Investigation. **Yuan Zhu:** Project administration, Formal analysis. **Yunchao Xiao:** Writing – review & editing, Supervision, Funding

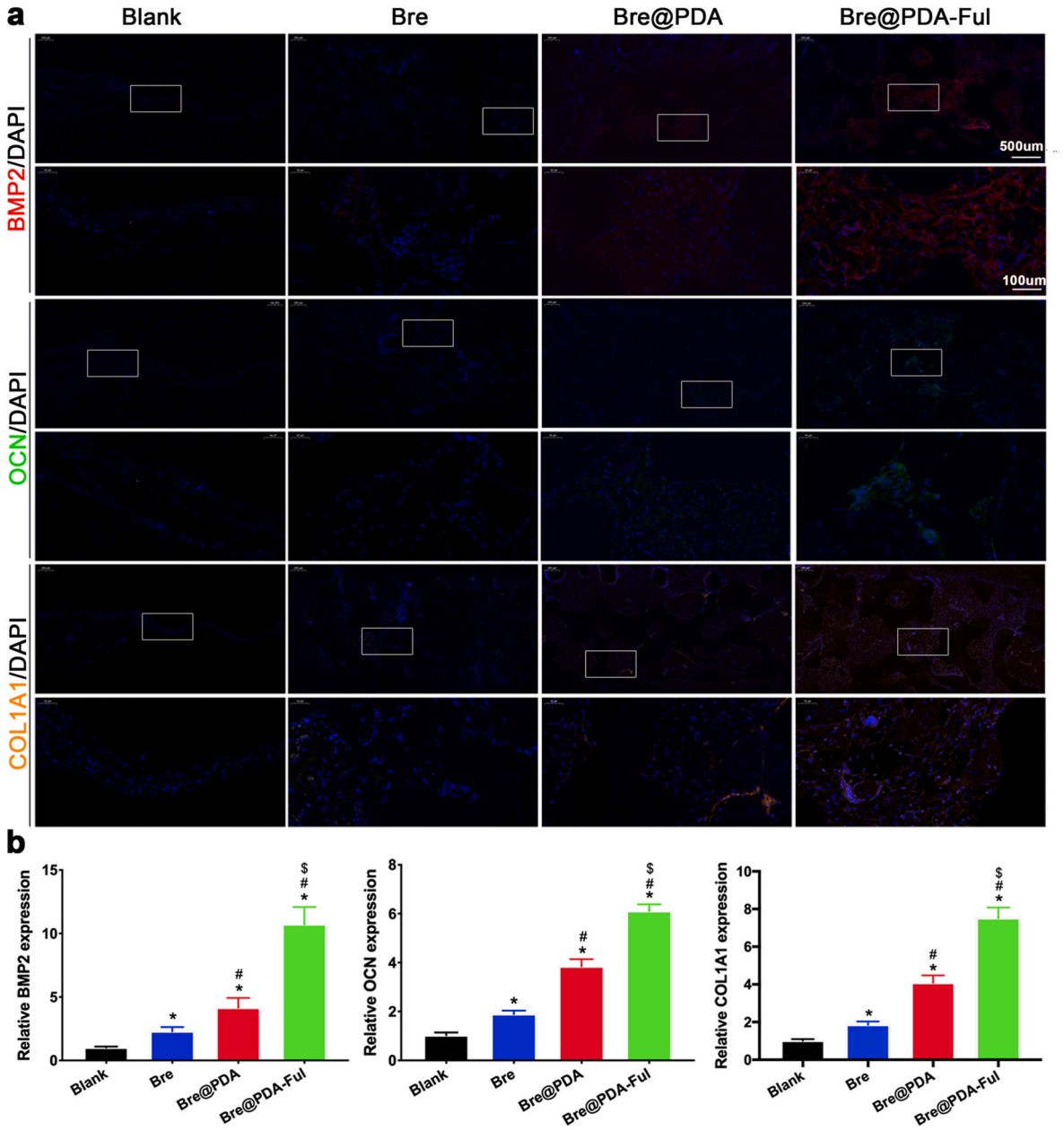

Fig. 8. Immunohistofluorescence detection of defect bone areas. a) Representative images indicating the expression of BMP2 (red), OCN (green), and COL1A1 (yellow) in the in defect bone areas of each group. b) Semi-quantitative assessment of the expression of BMP2, OCN, and COL1A1 in four groups. (*, #, and $ indicate $P < 0.05$ comparing to the Blank group, the Bre group, and the Bre@PDA group, respectively.). (For interpretation of the references to colour in this figure legend, the reader is referred to the Web version of this article.)

acquisition. **Xiangyang Xu:** Conceptualization.

Declaration of competing interest

The authors declare no conflict of interest.

Data availability

Data will be available on request.

Acknowledgements

This work was financially supported by National Natural Science Foundation of China (82202686), Shanghai Jiading District Health Committee (2022-QN-OS), Zhejiang Provincial Natural Science Foundation (LQ22C100002), Science and Technology Bureau of Jiaxing City (2023AD11042), Key Laboratory of Yarn materials Forming and Composite Processing Technology, Zhejiang Province (70722003-2207).

Appendix A. Supplementary data

Supplementary data to this article can be found online at https://doi.org/10.1016/j.mtbio.2024.101120.

References

[1] C.D. Buckley, C. Ospelt, S. Gay, K.S. Midwood, Location, location, location: how the tissue microenvironment affects inflammation in RA, Nat. Rev. Rheumatol. 17 (4) (2021) 195–212.

[2] Y. Hu, X. Chen, S. Wang, Y. Jing, J. Su, Subchondral bone microenvironment in osteoarthritis and pain, Bone Res. 9 (1) (2021) 20.
[3] J. Li, F. Han, J. Ma, H. Wang, J. Pan, G. Yang, H. Zhao, J. Zhao, J. Liu, Z. Liu, Targeting endogenous hydrogen peroxide at bone defects promotes bone repair, Adv. Funct. Mater. 32 (10) (2022) 2111208.
[4] B. Yang, Y. Chen, J. Shi, Reactive oxygen species (ROS)-Based nanomedicine, Chem. Rev. 119 (8) (2019) 4881–4985.
[5] H.T. Aiyelabegan, E. Sadroddiny, Fundamentals of protein and cell interactions in biomaterials, Biomed. Pharmacother. 88 (2017) 956–970.
[6] W.H. Chooi, S.Y. Chew, Modulation of cell-cell interactions for neural tissue engineering: potential therapeutic applications of cell adhesion molecules in nerve regeneration, Biomaterials 197 (2019) 327–344.
[7] J.E.P. Brouns, P.Y.W. Dankers, Introduction of enzyme-responsivity in biomaterials to achieve dynamic reciprocity in cell-material interactions, Biomacromolecules 22 (1) (2021) 4–23.
[8] Y. Yao, H. Zhang, Z. Wang, J. Ding, S. Wang, B. Huang, S. Ke, C. Gao, Reactive oxygen species (ROS)-responsive biomaterials mediate tissue microenvironments and tissue regeneration, J. Mater. Chem. 7 (33) (2019) 5019–5037. B.
[9] J.B. Lee, Y.M. Shin, W.S. Kim, S.Y. Kim, H.J. Sung, ROS-responsive biomaterial design for medical applications, Adv. Exp. Med. Biol. 1064 (2018) 237–251.
[10] F. Migliorini, G. La Padula, E. Torsiello, F. Spiezia, F. Oliva, N. Maffulli, Strategies for large bone defect reconstruction after trauma, infections or tumour excision: a comprehensive review of the literature, Eur. J. Med. Res. 26 (1) (2021) 118.
[11] G. Walters, I. Pountos, P.V. Giannoudis, The cytokines and micro-environment of fracture haematoma: current evidence, J. Tissue Eng. Regen. Med. 12 (3) (2018) e1662–e1677.
[12] G. Cerqueni, A. Scalzone, C. Licini, P. Gentile, M. Mattioli-Belmonte, Insights into oxidative stress in bone tissue and novel challenges for biomaterials, Mater. Sci. Eng. C. Mater. Biol. Appl. 130 (2021) 112433.
[13] I. Ozmen, M. Naziroglu, R. Okutan, Comparative study of antioxidant enzymes in tissues surrounding implant in rabbits, Cell Biochem. Funct. 24 (3) (2006) 275–281.
[14] F. Wauquier, L. Leotoing, V. Coxam, J. Guicheux, Y. Wittrant, Oxidative stress in bone remodelling and disease, Trends Mol. Med. 15 (10) (2009) 468–477.
[15] A.J. Sheppard, A.M. Barfield, S. Barton, Y. Dong, Understanding reactive oxygen species in bone regeneration: a glance at potential therapeutics and bioengineering applications, Front. Bioeng. Biotechnol. 10 (2022) 836764.
[16] J. Li, C. Deng, W. Liang, F. Kang, Y. Bai, B. Ma, C. Wu, S. Dong, Mn-containing bioceramics inhibit osteoclastogenesis and promote osteoporotic bone regeneration via scavenging ROS, Bioact. Mater. 6 (11) (2021) 3839–3850.
[17] J. Watanabe, M. Yamada, K. Niibe, M. Zhang, T. Kondo, M. Ishibashi, H. Egusa, Preconditioning of bone marrow-derived mesenchymal stem cells with N-acetyl-L-cysteine enhances bone regeneration via reinforced resistance to oxidative stress, Biomaterials 185 (2018) 25–38.
[18] W. Chen, X. Shen, Y. Hu, K. Xu, Q. Ran, Y. Yu, L. Dai, Z. Yuan, L. Huang, T. Shen, K. Cai, Surface functionalization of titanium implants with chitosan-catechol conjugate for suppression of ROS-induced cells damage and improvement of osteogenesis, Biomaterials 114 (2017) 82–96.
[19] T. Zhou, L. Yan, C. Xie, P. Li, L. Jiang, J. Fang, C. Zhao, F. Ren, K. Wang, Y. Wang, H. Zhang, T. Guo, X. Lu, A mussel-inspired persistent ROS-scavenging, electroactive, and osteoinductive scaffold based on electrochemical-driven in situ nanoassembly, Small (2019) e1805440.
[20] C. Wu, J. Chang, J. Wang, S. Ni, W. Zhai, Preparation and characteristics of a calcium magnesium silicate (bredigite) bioactive ceramic, Biomaterials 26 (16) (2005) 2925–2931.
[21] W. Zhang, C. Feng, G. Yang, G. Li, X. Ding, S. Wang, Y. Dou, Z. Zhang, J. Chang, C. Wu, X. Jiang, 3D-printed scaffolds with synergistic effect of hollow-pipe structure and bioactive ions for vascularized bone regeneration, Biomaterials 135 (2017) 85–95.
[22] S. Moazami, M. Kharaziha, R. Emadi, M. Dinari, Multifunctional bioinspired bredigite-modified adhesive for bone fracture healing, ACS Appl. Mater. Interfaces 15 (5) (2023) 6499–6513.
[23] Y. Shen, Z. Wang, J. Wang, Y. Zhou, H. Chen, C. Wu, M. Haapasalo, Bifunctional bioceramics stimulating osteogenic differentiation of a gingival fibroblast and inhibiting plaque biofilm formation, Biomater. Sci. 4 (4) (2016) 639–651.
[24] J. Grebowski, P. Kazmierska, A. Krokosz, Fullerenols as a new therapeutic approach in nanomedicine, BioMed Res. Int. 2013 (2013) 751913.
[25] R. Injac, M. Prijatelj, B. Strukelj, Fullerenol nanoparticles: toxicity and antioxidant activity, Methods Mol. Biol. 1028 (2013) 75–100.
[26] E.E. Fileti, R. Rivelino, F. Brito Mota, T. Malaspina, Effects of hydroxyl group distribution on the reactivity, stability and optical properties of fullerenols, Nanotechnology 19 (36) (2008) 365703.
[27] S. Osuna, M. Swart, M. Solà, On the mechanism of action of fullerene derivatives in superoxide dismutation, Chemistry (Weinheim an der Bergstrasse, Germany) 16 (10) (2010) 3207–3214.
[28] N. Tsao, T.Y. Luh, C.K. Chou, J.J. Wu, Y.S. Lin, H.Y. Lei, Inhibition of group A streptococcus infection by carboxyfullerene, Antimicrob. Agents Chemother. 45 (6) (2001) 1788–1793.
[29] J. Tang, R. Zhang, M. Guo, L. Shao, Y. Liu, Y. Zhao, S. Zhang, Y. Wu, C. Chen, Nucleosome-inspired nanocarrier obtains encapsulation efficiency enhancement and side effects reduction in chemotherapy by using fullerenol assembled with doxorubicin, Biomaterials 167 (2018) 205–215.
[30] X. Yang, L. Jin, L. Yao, F.H. Shen, A.L. Shimer, X. Li, Antioxidative nanofullerol prevents intervertebral disk degeneration, Int. J. Nanomed. 9 (2014) 2419–2430.
[31] K. Yudoh, K. Shishido, H. Murayama, M. Yano, K. Matsubayashi, H. Takada, H. Nakamura, K. Masuko, T. Kato, K. Nishioka, Water-soluble C60 fullerene prevents degeneration of articular cartilage in osteoarthritis via down-regulation of chondrocyte catabolic activity and inhibition of cartilage degeneration during disease development, Arthritis Rheum. 56 (10) (2007) 3307–3318.
[32] M. Seke, D. Petrovic, A. Djordjevic, D. Jovic, M.L. Borovic, Z. Kanacki, M. Jankovic, Fullerenol/doxorubicin nanocomposite mitigates acute oxidative stress and modulates apoptosis in myocardial tissue, Nanotechnology 27 (48) (2016) 485101.
[33] X. Yang, C.J. Li, Y. Wan, P. Smith, G. Shang, Q. Cui, Antioxidative fullerol promotes osteogenesis of human adipose-derived stem cells, Int. J. Nanomed. 9 (2014) 4023–4031.
[34] H. Geng, Y.N. Chang, X. Bai, S. Liu, Q. Yuan, W. Gu, J. Li, K. Chen, G. Xing, G. Xing, Fullerenol nanoparticles suppress RANKL-induced osteoclastogenesis by inhibiting differentiation and maturation, Nanoscale 9 (34) (2017) 12516–12523.
[35] H. Shao, M. Sun, F. Zhang, A. Liu, Y. He, J. Fu, X. Yang, H. Wang, Z. Gou, Custom repair of mandibular bone defects with 3D printed bioceramic scaffolds, J. Dent. Res. 97 (1) (2018) 68–76.
[36] H.J. Cha, D.S. Hwang, S. Lim, Development of bioadhesives from marine mussels, Biotechnol. J. 3 (5) (2008) 631–638.
[37] H. Lee, S.M. Dellatore, W.M. Miller, P.B. Messersmith, Mussel-inspired surface chemistry for multifunctional coatings, Science (New York, N.Y.) 318 (5849) (2007) 426–430.
[38] Y. Tian, Y. Cao, Y. Wang, W. Yang, J. Feng, Realizing ultrahigh modulus and high strength of macroscopic graphene oxide papers through crosslinking of mussel-inspired polymers, Adv. Mater. 25 (21) (2013) 2980–2983.
[39] T. Hao, J. Zhou, S. Lü, B. Yang, Y. Wang, W. Fang, X. Jiang, Q. Lin, J. Li, C. Wang, Fullerene mediates proliferation and cardiomyogenic differentiation of adipose-derived stem cells via modulation of MAPK pathway and cardiac protein expression, Int. J. Nanomed. 11 (2016) 269–283.
[40] Z. Zhou, K. Ni, H. Deng, X. Chen, Dancing with reactive oxygen species generation and elimination in nanotheranostics for disease treatment, Adv. Drug Deliv. Rev. 158 (2020) 73–90.
[41] D. LeBert, J.M. Squirrell, C. Freisinger, J. Rindy, N. Golenberg, G. Frecentese, A. Gibson, K.W. Eliceiri, A. Huttenlocher, Damage-induced reactive oxygen species regulate vimentin and dynamic collagen-based projections to mediate wound repair, Elife 7 (2018).
[42] H. Sies, D.P. Jones, Reactive oxygen species (ROS) as pleiotropic physiological signalling agents, Nat. Rev. Mol. Cell Biol. 21 (7) (2020) 363–383.
[43] S. Rizwan, P. ReddySekhar, B. MalikAsrar, Reactive oxygen species in inflammation and tissue injury, Antioxidants Redox Signal. 20 (7) (2014) 1126–1167.
[44] J. Zhang, Y. Fu, P. Yang, X. Liu, Y. Li, Z. Gu, ROS scavenging biopolymers for anti-inflammatory diseases: classification and formulation, Adv. Mater. Interfac. 7 (16) (2020) 2000632.
[45] X. Sun, X. Li, H. Qi, X. Hou, J. Zhao, X. Yuan, X. Ma, MiR-21 nanocapsules promote early bone repair of osteoporotic fractures by stimulating the osteogenic differentiation of bone marrow mesenchymal stem cells, J Orthop Translat 24 (2020) 76–87.
[46] V.O. Kaminskyy, B. Zhivotovsky, Free radicals in cross talk between autophagy and apoptosis, Antioxidants Redox Signal. 21 (1) (2014) 86–102.
[47] N. Yin, Z. Zhang, Y. Ge, Y. Zhao, Z. Gu, Y. Yang, L. Mao, Z. Wei, J. Liu, J. Shi, Z. Wang, Polydopamine-based nanomedicines for efficient antiviral and secondary injury protection therapy, Sci. Adv. 9 (24) (2023) eadf4098.
[48] F. Lao, L. Chen, W. Li, C. Ge, Y. Qu, Q. Sun, Y. Zhao, D. Han, C. Chen, Fullerene nanoparticles selectively enter oxidation-damaged cerebral microvessel endothelial cells and inhibit JNK-related apoptosis, ACS Nano 3 (11) (2009) 3358–3368.
[49] L.C. Cheng, X. Jiang, J. Wang, C. Chen, R.S. Liu, Nano-bio effects: interaction of nanomaterials with cells, Nanoscale 5 (9) (2013) 3547–3569.
[50] M. Ahmad, B.T. Krüger, T. Kroll, S. Vettorazzi, A.K. Dorn, F. Mengele, S. Lee, S. Nandi, D. Yilmaz, M. Stolz, N.K. Tangudu, D.C. Vázquez, J. Pachmayr, I. C. Cirstea, M.V. Spasic, A. Ploubidou, A. Ignatius, J. Tuckermann, Inhibition of Cdk5 increases osteoblast differentiation and bone mass and improves fracture healing, Bone Res. 10 (1) (2022) 33.
[51] S. Koo, B. König Jr., S. Allegrini Jr., M. Yoshimoto, M.J. Carbonari, F.F. Mitri-Luiz, Titanium implant osseointegration with calcium pyrophosphate in rabbits, J. Biomed. Mater. Res. B Appl. Biomater. 76 (2) (2006) 373–380.